ELSEVIER

Contents lists available at ScienceDirect

### Earth and Planetary Science Letters

journal homepage: www.elsevier.com/locate/epsl





# Permeability and seismicity rate changes at an inflating submarine volcano caused by dynamic stresses

Adnan Barkat <sup>a</sup>, Yen Joe Tan <sup>a,\*</sup>, Guangyu Xu <sup>b</sup>, Felix Waldhauser <sup>c</sup>, Maya Tolstoy <sup>d</sup>, William S.D. Wilcock <sup>d</sup>

- <sup>a</sup> Earth and Environmental Sciences Programme, The Chinese University of Hong Kong, Hong Kong S.A.R., China
- <sup>b</sup> Applied Physics Laboratory, University of Washington, Seattle, WA, USA
- <sup>c</sup> Lamont-Doherty Earth Observatory of Columbia University, Palisades, NY, USA
- <sup>d</sup> School of Oceanography, University of Washington, Seattle, WA, USA

#### ARTICLE INFO

#### Keywords: Dynamic earthquake triggering Transient stresses Volcanic inflation Permeability changes

#### ABSTRACT

Transient stresses from the passage of seismic waves are known to trigger earthquakes and cause crustal permeability changes. However, whether permeability change is a main driver of dynamic earthquake triggering remains debated. Our understanding of the characteristics of dynamic triggering in submarine volcanic environments is also limited due to the lack of offshore observations. Here, we utilize a high-resolution micro-seismicity catalog from July 2015 to July 2022 to evaluate the triggering response of Axial Seamount, an inflating and seismically active submarine volcano located in the northeast Pacific Ocean. We report statistically significant episodes of dynamic earthquake triggering for ~18 % of the teleseismic events investigated, which is comparable with subaerial tectonic and volcanic environments. We do not observe any obvious dependence of triggering rate on the amplitude of peak ground velocity. However, a comparison of the triggering rate and the cumulative magma volume shows that the triggering susceptibility might increase as the volcano becomes more critically stressed. Using data recorded by a temperature sensor in a black smoker, we compute the phase lag between hydrothermal vent-fluid temperature and tidal loading amplitude before and after the arrival of teleseismic waves to probe the relationship between permeability change and dynamic triggering. While the energy density thresholds for dynamic earthquake triggering and permeability change are comparable, both triggering and non-triggering observations show similar proportions of permeability changes. Our results suggest that permeability change induced by transient stresses might not be a necessary or primary mechanism that drives dynamic earthquake triggering.

#### 1. Introduction

Transient stresses caused by the passage of seismic waves are capable of triggering seismicity at far-field distances (Hill et al., 1993). This phenomenon is known as dynamic earthquake triggering, first reported following the 1992 Landers earthquake (Hill et al., 1993) and has been widely observed since (Gomberg et al., 2001; Miyazawa et al., 2005; Peng et al., 2010; van der Elst and Brodsky, 2010; Aiken and Peng, 2014; Cattania et al., 2017; Bell et al., 2021). In general, when dynamic earthquake triggering occurs during the passage of seismic waves, it can be explained by the Coulomb failure model, where it is a result of a temporary increase in the stress level of favorably oriented faults over their frictional failure thresholds due to the transient stresses (Freed,

2005; Hill et al., 2008). However, the Coulomb failure model is unable to directly explain dynamic earthquake triggering that occurs after the passage of teleseismic waves (Gomberg, 2001). Consequently, additional physical mechanisms have been proposed to explain this delay including the excitation of crustal fluids (Hill et al., 1993), subcritical crack growth (Brodsky et al., 2000), granular media (Johnson and Jia, 2005), cascade stress triggering (Marsan and Lengline, 2008; Aiken and Peng, 2014), rate-and-state friction law (Parsons, 2005), and triggered creep (Shelly et al., 2011). Laboratory experiments have successfully validated the initiation of some of these secondary processes by transient stresses (Brodsky and Prejean, 2005; Savage and Marone, 2008; Gonzalez-Huizar and Velasco, 2011). Nevertheless, there is still a lack of consensus about the dominant controlling mechanism.

E-mail address: yjtan@cuhk.edu.hk (Y.J. Tan).

 $<sup>^{\</sup>ast}$  Corresponding author.

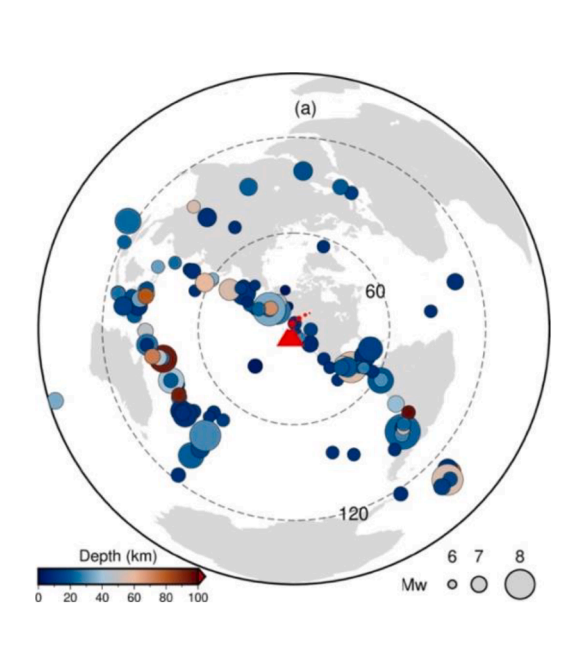
In particular, the excitation of crustal fluids by the passage of seismic waves is a mechanism that has received significant attention because it is also able to explain the observed propensity of volcanic and geothermal regions to dynamic earthquake triggering (Hill et al., 1993, 2008; Stark and Davis, 1996; Miyazawa et al., 2005; Prejean and Hill, 2018; Bell et al., 2021). Numerous processes including magmatic fluid movement, bubble formation, fracture growth, and permeability change can lead to the excitation of crustal fluids (Prejean and Hill, 2018; Seropian et al., 2021; Bell et al., 2021; Kinoshita et al., 2022). Among them, permeability changes have been frequently reported at both near and far-field distances after major earthquakes (Elkhoury et al., 2006; Manga et al., 2012; Shi et al., 2018, 2019; Liao et al., 2021). For example, Shi et al., (2018) reported a decrease in fault zone permeability in a hydrothermal system following large distant earthquakes. Moreover, Shi et al., (2019) discussed the potential dependence of permeability change on dynamic stress orientation. Furthermore, earlier studies also reported temperature changes in deep-ocean hydrothermal system following distant earthquakes and inferred this to have resulted from earthquake-induced permeability changes (Johnson et al., 2001; Dziak et al., 2003). Nevertheless, the connection between permeability change and dynamic earthquake triggering is still not well-elucidated due to the absence of concurrent observations of both permeability and seismicity rate changes.

Existing field observations and laboratory experiments have indicated that micro-seismicity can become more responsive to dynamic stress perturbations as a fault system becomes critically stressed (Savage and Maron, 2008; Tanaka, 2004; van der Elst et al., 2013a; Ide et al., 2016; Tan et al., 2018; Bell et al., 2021). For instance, Tanaka (2004) observed strengthening of earthquake tidal triggering signals in the Sumatra subduction zone leading up to three Mw > 8.5 earthquakes,

which vanished after these events. Likewise, van der Elst et al. (2013a) reported a high dynamic earthquake triggering rate at sites where fluid injections promoted fault failure. However, contradictory observations also exist. For example, van der Elst et al. (2013b) reported limited evidence of dynamic earthquake triggering in regions at the very beginning or end of their inferred seismic cycle. Since it is still not well-understood how earthquake triggering rate varies with changes in the background stress state, further studies are necessary to better comprehend the underlying dependence between background stress state and dynamic triggering potential.

Axial Seamount is a seismically active submarine volcano in the northeast Pacific Ocean which has had three major eruptions since 1998 (Fig. 1a) (Wilcock et al., 2016). It is seated at a depth of ~1.6 km below sea level with an elongated caldera (8  $\times$  3 km<sup>2</sup>) and an outward dipping ring-fault system. It also hosts high-temperature hydrothermal vent-fluid fields (Wilcock et al., 2018). Since late 2014, Axial Seamount hosts an advanced cabled volcanic observatory with a network of seismic and geodetic instruments and a hydrothermal vent-fluid high temperature sensor (Fig. 1b). Following the 2015 eruption, the geodetic observations reveal an increasing inflation rate of the shallow magma chamber (~1.5-2.5 km below seafloor) which is tightly linked to the rate of seismicity (Chadwick et al., 2022). In addition, Tolstoy et al. (2002) first reported a strong correlation between tides and micro-seismicity rate at Axial Seamount, which has been further investigated by Wilcock et al. (2016) and Scholz et al. (2019). The long observational record and demonstrated sensitivity to small stress perturbation make Axial Seamount a promising site to quantify the response of a magmatically robust and seismically active submarine volcanic system to dynamic stresses as it builds up to the next eruption.

In this study, we investigate how dynamic earthquake triggering at



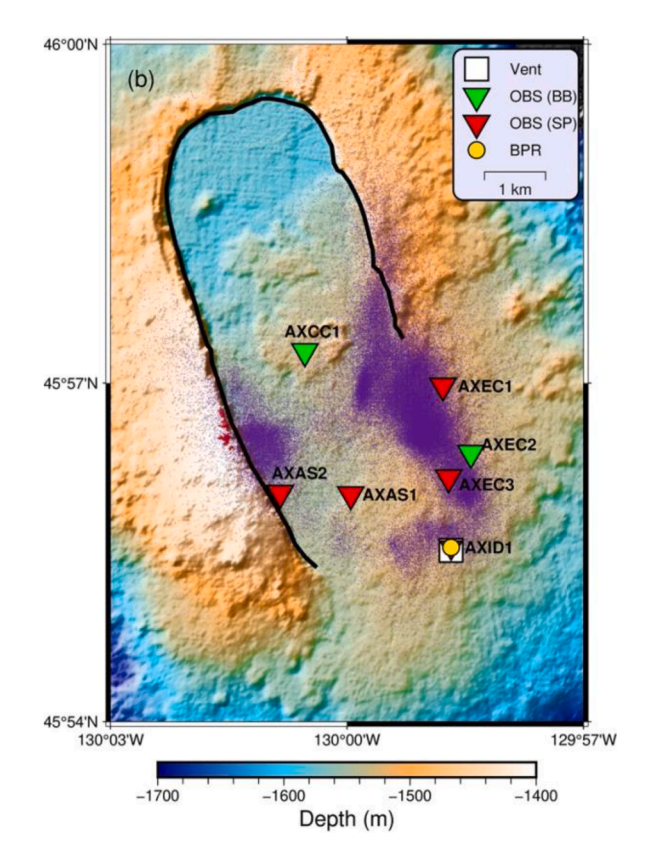


Fig. 1. (a) The spatial distribution of candidate earthquakes (coloured circles) relative to Axial Seamount (red triangle). Dashed circles represent distance in degree. (b) Zoom-in view of Axial Seamount's bathymetry, caldera rim (black line), and local seismicity (purple dots). Inverted triangles mark the locations of broadband (green) and short-period (red) ocean bottom seismometers along with the station names. Station AXID1, a hydrothermal vent-fluid temperature sensor (white square), and a bottom-pressure recorder (yellow circle) are located in close proximity with one another. (For interpretation of the references to color in this figure legend, the reader is referred to the web version of this article.)

Axial Seamount relates to its time-varying background stress state and the possible influence of permeability changes due to transient stresses. For this purpose, we analyze the micro-seismicity record from July 2015 to July 2022 to quantify Axial Seamount's triggering susceptibility as it re-inflates after the April 2015 eruption and approaches its next eruption. We further evaluate how the dynamic earthquake triggering might relate to permeability changes inferred from phase-lag observations of hydrothermal Vent-fluid Temperature and Tidal Pressure (VTTP). Our findings provide important insights into the dynamic triggering response of an active submarine volcanic system and its underlying physical mechanisms.

#### 2. Data and methods

#### 2.1. Axial Seamount local earthquake catalog

In late 2014, a state-of-the-art cabled observatory was established by the Ocean Observatories Initiative (OOI) at Axial Seamount to study underwater volcanism and accompanying processes (Kelley et al., 2014). For micro-seismicity monitoring, a network of Ocean Bottom Seismometers (OBSs: 6 short-period and 3 broadband) is installed around the southern half of the caldera (Fig. 1b). Recorded waveform data is transmitted to the Data Management Center (DMC) of the Incorporated Research Institutions for Seismology (IRIS) in real time. The continuous seismic data is processed (Wilcock et al., 2016) to detect earthquakes using short-term to long-term RMS triggering (Allen, 1978), pick arrival times with the Kurtosis method (Baillard et al., 2014) and locate earthquakes using Hypoinverse (Klein, 2002) with a 1D velocity model. Waldhauser et al. (2020) has subsequently implemented the real-time double-difference (RT-DD) approach (Waldhauser, 2009) to produce a high-resolution relocated catalog. In this study, we utilized the high-resolution relocated earthquake catalog from Waldhauser et al. (2020) covering the period from July 2015 to July 2022, subsequent to the 2015 eruption. This includes ~54,000 earthquakes occurring around Axial Seamount's caldera (Fig. 1b, 3a) with a completeness magnitude of Mw 0 (Tan et al., 2019).

#### 2.2. Candidate earthquakes

To select potential triggering sources that resulted in substantial dynamic but minimal static stress changes at Axial Seamount, we search for all earthquakes in the U.S. Geological Survey catalog during the posteruption period with  $M_w \geq 6.0$ , depth < 100 km, and distance > 100 km. Afterward, we define a quantity Q (a ratio of seismic moment  $M_o$  and distance d), and use  $Q < 10^{15}$  Joule/km as a threshold to remove events that do not generate sufficient dynamic stresses at Axial Seamount after accounting for the influence of geometric spreading of surface wave (Cattania et al., 2017). Furthermore, we also inspect the broadband OBS waveform records of the selected events and discard events with missing data or indistinguishable surface wave arrivals.

After initial screening, we compute the predicted surface wave arrivals using 5 km/s as the maximum surface wave speed of the potential triggering sources (Yun et al., 2019). These predicted arrivals are used to calculate the arrival time differences ( $\Delta t$ ) between temporally adjacent earthquakes. Two events are designated as 'connected' if  $\Delta t < 2$  hours (8 triggering sources are designated as connected events). For connected events, it is often very challenging to quantify the contribution of each event to the initiation of dynamically triggered seismicity. Therefore, we select the event with maximum Peak Ground Velocity (PGV) and consider it as the potential triggering source and discard the other event. In total, we are left with 146 Candidate Earthquakes (CE) with Mw between 6 and 8.3 to test whether they remotely triggered seismicity at Axial Seamount (Fig. 1a, Table S1).

We also utilized the waveform records of the three broadband OBS stations (Fig. 1b) to measure the PGV and frequency content of the surface waves. We first apply preliminary processing including

instrumental response removal, demeaning, and detrending. Afterward, we apply a 0.01–0.05 Hz band-pass filter to improve the visibility of low-frequency teleseismic surface waves (Fan et al., 2021). The filtered waveforms are then used to measure the PGV ( $\mu$ m/s). To obtain a representative PGV value, we average the PGVs measured at all three broadband OBS stations (Table S1). We also compute the velocity spectra of the filtered vertical-component waveform records to examine possible dependence of dynamic triggering on the frequency content of surface waves (Peng et al., 2010; Aiken and Peng, 2014; Fan et al., 2021).

#### 2.3. Identification of seismicity rate changes

To quantify the triggering response of Axial Seamount, we compute the seismicity rate change using the  $\beta$ -statistic method proposed by Matthews and Reasenberg (1988), which is widely used for detecting dynamic earthquake triggering (Gomberg et al., 2001; Aiken and Peng, 2014; Cattania et al., 2017; Bell et al., 2021). The  $\beta$ -statistic is defined as:

$$\beta = \left(N_a - N_b \times \frac{t_a}{t_b}\right) / \sqrt{N_b \times \frac{t_a}{t_b}}$$

where  $N_a$  is the earthquake count within the time window of interest  $(t_a)$ , while  $N_b$  represents the event count during a reference window  $(t_b)$ . The resultant  $\beta$  value shows the seismicity rate change during the time window of interest compared to the background seismicity rate. A positive  $\beta$  value indicates an increase in seismicity rate, while a negative  $\beta$  value indicates a decrease. Typically,  $\beta \geq 2$  is adopted as an indicator of the statistically significant increase in seismicity rate (Marsan and Wyss, 2011). However, in volcanic environments, the background seismicity rate can vary in response to underlying magmatic processes (Prejean and Hill, 2018), therefore a fixed threshold may not be appropriate for Axial Seamount. Consequently, we adopt the multi-threshold  $\beta$  approach to identify a statistically significant increase in seismicity rate (Fan et al., 2021), instead of using a fixed threshold.

In the multi-threshold  $\beta$  approach (Fan et al., 2021), we calculate the pre  $(\beta_b)$ - and post  $(\beta_0)$  surface waves arrival seismicity rate change for different  $t_a$  (2, 6, 12, and 24 hours immediately before and after the surface wave arrival) against a fixed  $t_b$  ( $\pm 3$ ,  $\pm 5$  days, whereas 0 marks the predicted surface wave arrivals). Here, the change in seismicity rate within t<sub>a</sub> = 2 hours is defined as 'instant triggering', whereas the other time windows ( $t_a = 6, 12, 24$  hours) are defined as 'delayed triggering'. Events with both instant and delayed triggering are termed as 'extended triggering. The  $\beta_h$  threshold ( $\beta_0 \ge \beta_h$ ) prevents us from falsely defining a seismicity rate increase that started before the surface waves arrival as dynamic earthquake triggering. Furthermore, to evaluate the significance of  $\beta_0$ , we calculate the  $\beta$ -statistic for 10,000 random  $t_a$  selected from within  $\pm 3$  days, and construct a random distribution- $\omega$ . We select a  $\beta$  threshold ( $\beta_{95\%}$ ) within the distribution- $\omega$  that exceeds 95 % of the population. The  $\beta_{95\%}$  threshold ( $\beta_0 \geq \beta_{95\%}$  ) verifies the statistical significance of  $\beta_0$  i.e. that the increase in seismicity rate immediately after the surface wave arrival is above 2 times of standard deviation of random occurrences. To evaluate the significance of the background seismicity, we calculate the  $\beta$ -statistic for 10, 000 random  $t_b$  (6 days' time window) selected from  $a \pm 30$  days window against  $t_a$  (2, 6, 12, and 24 hours immediately after the surface wave arrival), and construct a random distribution- $\gamma$ . We select a  $\beta$  threshold ( $\beta_{5\%}$ ) within the distribution- $\gamma$  that exceeds 5 % of the population. The  $\beta_{5\%}$  threshold can help to remove potential false detections due to low background seismicity rate. In other words, the  $\beta_{5\%}$  threshold confirms that the reference window  $t_b$  has sufficient seismicity for a reliable dynamic triggering test with reference to the long-term background seismicity rate. A candidate earthquake is classified as a triggering case if any one of the given triggering windows (2, 6, 12, 24 hours) has  $\beta_0 \geq \beta_b, \; \beta_0 \geq \beta_{95\%}$  and  $\beta_0 \geq \beta_{5\%}$ . An example representation of the multi-threshold  $\beta$  approach used to capture the seismicity rate changes is illustrated in Fig. 2. In this

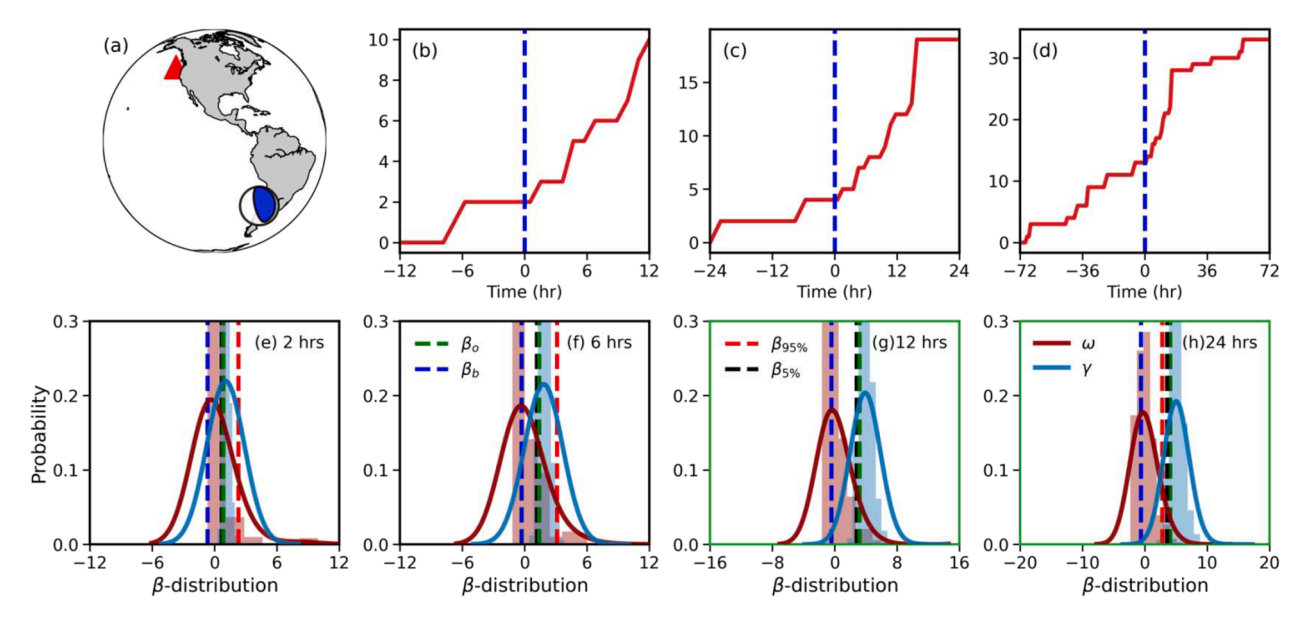


Fig. 2. Schematic representation of the multi-threshold  $\beta$  approach. (a) Illustrates the candidate earthquake location and focal mechanism, and Axial Seamount's location (red triangle). (b-d) Cumulative earthquake count for 3 time windows with vertical dashed lines representing the arrival time of teleseismic surface wave. (e-h) Random  $\beta$ -distributions and thresholds for different time windows used to identify seismicity rate changes (e-h). Green box panels mark the time windows with statistically significant increase in seismicity rate (g-h), whereas the black box panels mark the time windows without statistically significant increase in seismicity rate (e-f). (For interpretation of the references to color in this figure legend, the reader is referred to the web version of this article.)

particular case, the 12- and 24-hour (Fig. 2g-h) windows have  $\beta_0$  above all thresholds hence a statistically significant triggering case is declared.

## 2.4. Measurement of phase-lag between hydrothermal vent-fluid temperature and tidal amplitude

Periodic tidal loading modulates deep-sea hydrothermal venting which can provide important constraints on the properties of the oceanic crust (Wang and Davis, 1996; Crone and Wilcock, 2005; Barreyre et al., 2022). The phase-lag between VTTP records has been used to infer the effective permeability of the sub-surface layers at various submarine volcanic systems (Barreyre and Sohn, 2016; Xu et al., 2017; Barreyre et al., 2022). Here, we measure the change in phase-lag between the VTTP signals (M2-tidal component) to test the hypothesis of permeability change as a proposed mechanism for dynamic earthquake triggering (Elkhoury et al., 2006; Kinoshita et al., 2015, Liao et al., 2021). We utilized the VTTP datasets recorded at Axial Seamount from July 2015 to July 2022 (Figs. 1-S1). The hydrothermal vent-fluid temperature is recorded by a high temperature sensor with a sampling rate of 1 observation/minute in a black smoker at the International District hydrothermal field site located near the AXID1 OBS (Fig. 1b) The tidal loading data is acquired by a Bottom Pressure Recorder (BPR) with 1 observation/minute sampling rate co-located with the AXID1 OBS (Fig. 1b). We examined the 7-year record and performed quality control by removing time windows with data gaps, glitches, and/or inconsistent records exhibiting unrealistic values or sharp jumps in values.

We used the cross-correlation method to measure the phase-lag between the VTTP signals (Azaria and Hertz, 1984). Initially, we divide the VTTP dataset into short segments ( $\pm$  5 days) around surface waves arrival time of the CE's and discard segments with data gaps. The schematic illustration of the phase-lag computation is provided in Fig. S1. To quantify the phase-lag fluctuations, uncertainties, and potential systematic trend within the short segments of the VTTP dataset, each segment is further subdivided into smaller overlapping (1-day overlap) intervals of 2-days lengths. The phase-lag is computed for each 2-day window along with the cross-correlation coefficient (ranges between 0 and 1), which indicates the signal quality. Afterward, we demean, detrend, and filter (1–4 cycle/day) the VTTP data to suppress

the noise. Then, we discard phase-lag measurements with a cross-correlation coefficient lower than 0.7 to ensure only good quality observations are incorporated. Finally, we compute the mean and standard deviation of the phase-lag observations before and after the arrival of seismic waves, and declare an increase or decrease of phase-lag based on the difference in mean phase-lag observations ( $\Delta$ -lag). We infer an increase in permeability from negative  $\Delta$ -lag observations and vice versa (Barreyre et al., 2022). If the  $\Delta$ -lag is lower than the standard deviation of the phase-lag observations before and after the arrival of the teleseismic waves ( $\pm$  5 days window), we infer this to represent no change in permeability (null cases). Based on the aforementioned set of criteria, we are left with 44 phase-lag measurements (Table S1) to quantify the possible influence of transient stresses on permeability changes.

Following the aforementioned approach, we randomly resample 100 time windows (10-day long) from July 2015 to June 2019 (afterward VTTP data is not stable) and compute  $\Delta$ -lag within smaller overlapping (1-day) 2-day long intervals to evaluate the significance of our  $\Delta$ -lag observations. We report ~24 % cases of changed and ~76 % cases of null  $\Delta$ -lag observations, respectively. Furthermore, we also select 11 clean segments of VTTP dataset of ~1 month duration to analyze the long term temporal variation in phase lag. The selected segments are further sub-divided into 3-day overlapping (1 day) windows. Subsequently, we apply the cross-correlation method to compute the phase lag for each window along with the cross-correlation coefficient. We only utilize phase lag observations having a cross-correlation coefficient >0.7 to ensure only good quality observations are incorporated. Afterward, we compute the mean and standard deviation of phase lag observations for each month-long segment and then compare it with the deformation time series (Fig. S2). We observe that the phase-lag is generally inversely correlated with inflation (Fig. S2), which is consistent with an increase in permeability due to the opening of cracks as the edifice is under extensional volumetric strain. Moreover, we also compare our long-term phase lag observation computed via the cross-correlation method with the results using the coherence approach adopted by Barreyre et al. (2014). The observed consistency among the phase lag values (Fig. S2) verifies the applicability of the cross-correlation method for estimating phase lag changes which are then used to infer permeability changes

(Fig. S2).

#### 3. Results

#### 3.1. How Axial Seamount responds to dynamic stresses

Following the multi-threshold β approach, we identify 26 statistically significant cases (~18 % of the CE) of dynamic triggering at Axial Seamount (Table S1). Of these 26 triggering cases, we identify 3, 15, and 8 cases of instant, delayed, and extended triggering, respectively (Table S1). We further inspect the waveforms of both instant and extended triggering cases to identify the triggering during the surface waves' arrival. We found that the dynamically triggered seismicity are randomly distributed and do not preferentially coincide with the maximum surface wave amplitude. Fig. 3b shows the temporal distribution of triggering and non-triggering cases against the measured vertical-component PGV and the magnitude of the earthquakes. In general, we do not observe any clear dependence of spatiotemporal triggering rate on the PGV amplitude and the earthquake magnitude (Figs. S3-S4). For example, the triggering rate for CEs with 100 < PGV < $1000 \,\mu\text{m/s}$  (35.71 %; Fig. S3b) is higher than both the CEs with PGV > $1000 \mu m/s$  (25 %; Fig. S3c) and PGV <  $100 \mu m/s$  (15.62 %; Fig. S3a). However, the number of CEs with PGV  $\geq$ 1000  $\mu$ m/s is too small to obtain a reliable estimate of the triggering rate.

To look for potential triggering dependence on the orientation of the incoming seismic waves, we compare the azimuthal direction of both triggering and non-triggering CE (Fig. S5; Table S2). However, due to the uneven distribution of CE for different azimuthal bands, we are not able to reliably determine the triggering rate for all azimuthal orientations. Therefore, we grouped the CE into  $20^\circ$  bins of azimuthal angles. We only select bins with a sufficient number of CE ( $\geq$  5). We observe that the triggering rate is ~30 % for azimuths ~130° and ~230°, whereas the typical triggering rate for the other azimuths is ~10–15 % (Table S2, Fig. S5). However, due to limited observations within each bin, we cannot quantify its robustness. Furthermore, we also investigate potential triggering dependence on the frequency content of the CE by comparing the average frequency spectra of triggering and non-triggering CE (Fig. S6). The frequency spectra of triggering and non-triggering CE's are indistinguishable.

#### 3.2. How triggering rates change as Axial Seamount inflates

To evaluate whether the triggering rate is influenced by the background stress level, we have to constrain the influence of other potential controlling factors such as amplitude of incoming seismic waves and background seismicity rate. To account for potential biases associated with the dynamic stress amplitude, we perform PGV normalization. For PGV normalization, we grouped the CE based on their PGV values: (1)

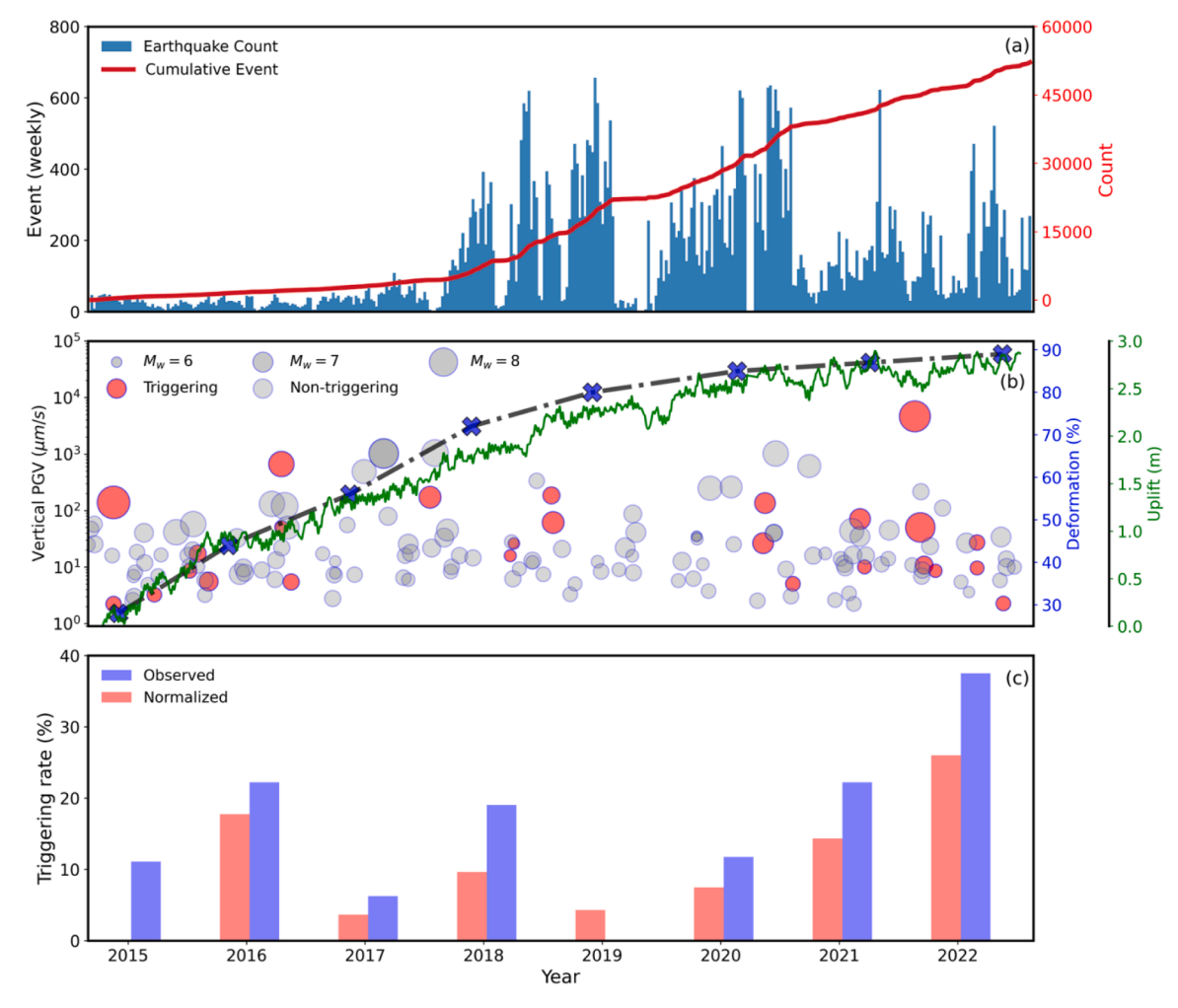


Fig. 3. (a) Light-blue histogram shows weekly earthquake counts. Solid-red line represents the cumulative earthquake count over the study period. (b) Illustrates the temporal distribution of triggering (red circles) and non-triggering (gray circles) cases scaled with their PGV from July 2015 to July 2022. Blue cross-marks denote the change in deformation relative to the 2015 pre-eruption level, whereas dashed-dotted line exhibits overall trend. The absolute uplift relative to 2015 posteruption level is indicted by green solid line. (c) Comparison of the observed and normalized triggering rate as a function of time. (For interpretation of the references to color in this figure legend, the reader is referred to the web version of this article.)

PGV  $\leq 100~\mu m/s$ , and (2) PGV  $> 100~\mu m/s$  under the assumption that the stress amplitude within each group is comparable. To minimize the possible influence of the higher PGV on the triggering rate, we only consider CE with PGV  $\leq 100~\mu m/s$  and ignore CE with higher PGV due to the small proportion of events (Fig. S3). To account for potential biases associated with the non-uniform background seismicity rate, we apply seismicity normalization. We select the year with the lowest annual earthquake count (2015) and scale down the earthquake count for each year (2016–2022) to the same level through random sampling of the catalog. Eventually, we are left with an equal number of earthquakes for each year to perform a reliable estimate of the temporal triggering susceptibility.

Subsequently, we compute and compare the annual triggering rate using both the original and normalized catalogs (Fig. 3c). We find that the triggering rate using the normalized catalog is lower than the triggering rate using the original catalog (except for 2019), but the trend remains consistent. The triggering rate fluctuates between 2015–2018, and starting from 2019 and extending through 2022, it exhibits an increase over time (Fig. 3c). To analyze the possible dependence of the triggering rate on the time-varying background stress state due to the underlying inflating magmatic body, we compare the cumulative deformation relative to the 2015 pre-eruption level (Chadwick et al., 2022) with the triggering rate (Figs. 3c). We report a consistent increase in the triggering rate after Axial Seamount's inflation reached ~80 % of the 2015 pre-eruption level (Fig. 3).

#### 3.3. How permeability changes relate to dynamic earthquake triggering

We analyze the phase-lag observations of VTTP for triggering and non-triggering CEs to test the hypothesis of permeability change as an underlying mechanism of dynamic earthquake triggering. A schematic illustration of phase-lag fluctuation before and after the arrival of surface waves is presented in Fig. 4. The Fig. 4a is an example of a decrease in phase-lag (increase in permeability) after the arrival of surface waves, whereas Fig. 4b is an example of unchanged phase-lag observations. We analyze the distribution of the  $\Delta$ -lag observations to evaluate how crustal permeability is influenced by the teleseismic surface waves. We observe both changed ( $\sim$ 70 %) and null ( $\sim$ 30 %)  $\Delta$ -lag cases despite

comparable PGV amplitude and surface waves duration (Fig. S7). Intriguingly, the changed  $\Delta$ -lag observations also include both positive and negative values. However, the proportion of negative  $\Delta$ -lag observations (68 %) is significantly higher than positive (32 %) observations (Fig. S7). A comparison of the frequency spectra of surface waves for both positive and negative  $\Delta$ -lag observations does not show any dependence of  $\Delta$ -lag on the frequency content of the surface waves (Fig. S8). We further compare the  $\Delta$ -lag fluctuations with the orientation of the incoming seismic waves to analyze the  $\Delta$ -lag dependence on the azimuthal distribution of the CE (Fig. S9). Due to the uneven distribution of CE, we only consider three azimuthal bands (~135°  $\pm$  20°, 240°  $\pm$  $20^{\circ}$ , and  $315^{\circ} \pm 20^{\circ}$ ) with enough observations ( $\geq 5$  CE). Among them, the proportion of changed  $\Delta$ -lag observation is  $\sim$ 70 % for azimuthal bands of  $\sim 135^{\circ}$  and  $\sim 240^{\circ}$ , and  $\sim 55$  % for azimuth  $\sim 315^{\circ}$  (Fig. S9; Table S3). In addition, we also observe that the positive  $\Delta$ -lag observations are dominantly concentrated (~62 %; 5/8) within the 240°  $\pm$ 20° azimuthal band, whereas other azimuthal bands show a relatively higher proportion of negative  $\Delta$ -lag observations (~80 %; 8/10 for azimuthal band  $\sim 135^{\circ} \pm 20^{\circ}$ ), respectively (Fig. S9c).

To evaluate how dynamic earthquake triggering might be related to permeability changes, we compare the frequency distribution of  $\Delta$ -lag observations for both triggering and non-triggering cases (Fig. 4c-d). For triggering cases, we observe the proportion of null  $\Delta$ -lag observations (~38 %) is lower than the changed (~62 %) observations, which include both positive (20 %) and negative (80 %) values (Fig. 4c). We find that long-duration surface waves are associated with negative  $\Delta$ -lag values, whereas positive  $\Delta$ -lag values are dominantly associated with short-duration surface waves. However, both appear to be independent of PGV amplitude (Fig. 4e). Likewise, the proportion of the null  $\Delta$ -lag observations (~25 %) is considerably lower than the changed observations (~75 %) for non-triggering cases which include both positive (~25 %) and negative (~75 %) values (Fig. 4d). We did not observe any clear dependence of  $\Delta$ -lag observations on the PGV and surface waves duration for non-triggering cases (Fig. 4f).

#### 4. Discussion

Volcanic and geothermal regions have been suggested to be

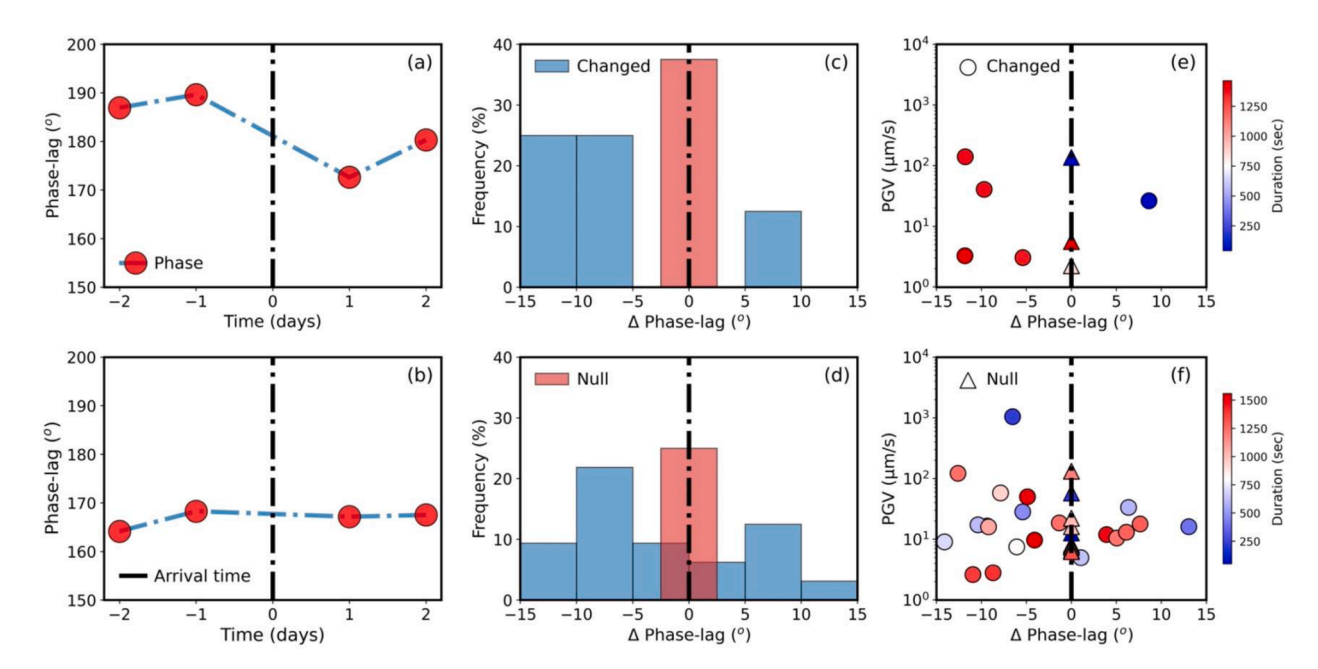


Fig. 4. Illustration of the phase-lag observations used to infer permeability changes. Examples of (a) decreasing and (b) stable phase-lag observations around the arrival time of the surface waves (vertical black dash dotted line). Frequency distribution of the phase-lag observations for (c) triggering and (d) non-triggering cases. Phase-lag dependence on the PGV and duration of the surface waves for (e) triggering and (f) non-triggering cases. Triangles indicate cases of no phase lag changes (null observations).

particularly susceptible to dynamic earthquake triggering due to the excitation of crustal fluids (Hill et al., 1993, 2008; Miyazawa et al., 2005; Stark and Davis, 1996; Bell et al., 2021), though exceptions also exist (Harrington and Brodsky, 2006; Velasco et al., 2008; Parsons and Velasco, 2011; Prejean and Hill, 2018). For instance, Aiken and Peng (2014) reported weak triggering response of volcanic and geothermal regions (2–6.8 %) in comparison with tectonic regions ( $\sim$ 9.2 %), despite comparable stress amplitude. They argued that the varying triggering behaviour (Long Valley Caldera ~2.0 %, Coso Geothermal Field ~3.8 %, and Geysers Geothermal Field  $\sim\!6.8$  %) likely reflects how close the faults are to failure. On the other hand, Fan et al. (2021) and Alfaro-Diaz et al. (2020) reported comparable triggering rates (~20 %) for tectonic and geothermal regions, whereas Prejean and Hill (2018) corroborated that the weak and variable response of Alaskan volcanoes is presumably due to the time-varying crustal conditions such as the stress state and pore-pressure distribution.

We find that  $\sim$ 18 % of CEs show dynamic earthquake triggering at Axial Seamount which is considerably higher than many previous observations in volcanic regions (Harrington and Brodsky, 2006; Aiken and Peng, 2014; Prejean and Hill, 2018; Pankow and Kilb, 2020). While these studies applied different approaches to the selection of triggering sources and/or triggering detection, our observed triggering rate of ~18 % is comparable with Fan et al. (2021). They used a similar workflow for triggering detection and observed a ~20 % triggering rate from both tectonic and geothermal regions in California. We further evaluated the robustness of our estimated triggering rate by lowering the detection threshold of  $\beta_{95\%}$  threshold to a 90 % confidence interval and find insignificant change in triggering rate (increased from  $\sim$ 18 % to  $\sim$ 20 %) (Tables S1). We also compare our triggering observations with previous studies at various volcanic and tectonic regions for a range of magnitude and epicentral distances with energy density (E) (Moran et al., 2004; Miyazawa et al., 2005; Cannata et al., 2010; Peng et al., 2010; Wu et al., 2011; Yukutake et al., 2013; Chao et al., 2013; Aiken and Peng, 2014; Kundu et al., 2016; Mendoza et al., 2016; Cattania et al., 2017; Neves et al., 2018; Alfaro-Diaz et al., 2020; Fan et al., 2021). We find that the triggering response of Axial Seamount is comparable with the other environments considering the event magnitude, epicentral distance, and E (Fig. 5a). Therefore, our observations suggest that Axial Seamount has a similar sensitivity to dynamic earthquake triggering in comparison with subaerial tectonic and volcanic regions.

Dependence of the triggering rate on the dynamic stress amplitude is often not clearly discernible in previous studies (Brodsky and Prejean, 2005; Aiken and Peng, 2014; Aiken et al., 2018; Fan et al., 2021). For example, Aiken and Peng (2014) reported varying triggering thresholds in different volcanic and geothermal regions despite comparable stress amplitude, presumably due to the varying background stress state. Likewise, we did not observe any clear dependence of triggering on stress amplitude, which suggests that stress amplitude may not be the primary controlling factor. In comparison, we find that the triggering rate at Axial Seamount is potentially higher for azimuth  ${\sim}230^{\circ}\,\pm\,10^{\circ}$ (triggering rate=30.77 %; Fig. S5, S9; Table S2), perpendicular to the local fault orientation (~330°) (Levy et al., 2018). Likewise, Alfaro-Diaz et al. (2020) also reported higher sensitivity of dynamic triggering for azimuths perpendicular to the local stress field. With this, we hypothesize that dynamic earthquake triggering at Axial Seamount might be sensitive to the orientation of the incoming seismic waves. Given our limited azimuthal coverage, more observations are required to elucidate the relation between dynamic triggering, and stress orientation. Finally, we did not observe any clear difference between the frequency spectra of triggering and non-triggering CE, which suggests that dynamic triggering at Axial Seamount is not particularly sensitive to the frequency content of the incoming seismic waves (Fig. S6).

We attempt to test whether the time-varying background stress state due to the inflating magma chamber influences the triggering susceptibility of Axial Seamount. Notably, we observe a lack of clear temporal trend of the triggering rate during the post-eruption period from 2015–2019 (Fig. 3). The variable triggering rate during the immediate post-eruption period could be due to the complex stress field and heterogeneous slip pattern as demonstrated by Levy et al. (2018), though the slip patterns after Dec 2016 are not known. Starting in 2019, we see a consistent increase in triggering rate over time which coincides with the cumulative magma volume having reached 80 % of the 2015 pre-eruption level (Chadwick et al., 2022). This suggests that Axial Seamount might be critically stressed beyond this inflation level hence is increasingly sensitive to dynamic earthquake triggering. We also observed that the proportion of instant/extended and delayed triggering rates varies over time. For instance, the proportion of instant/extended and delayed triggering were  $\sim 15$  % (2/14) and  $\sim 84$  % (12/14)

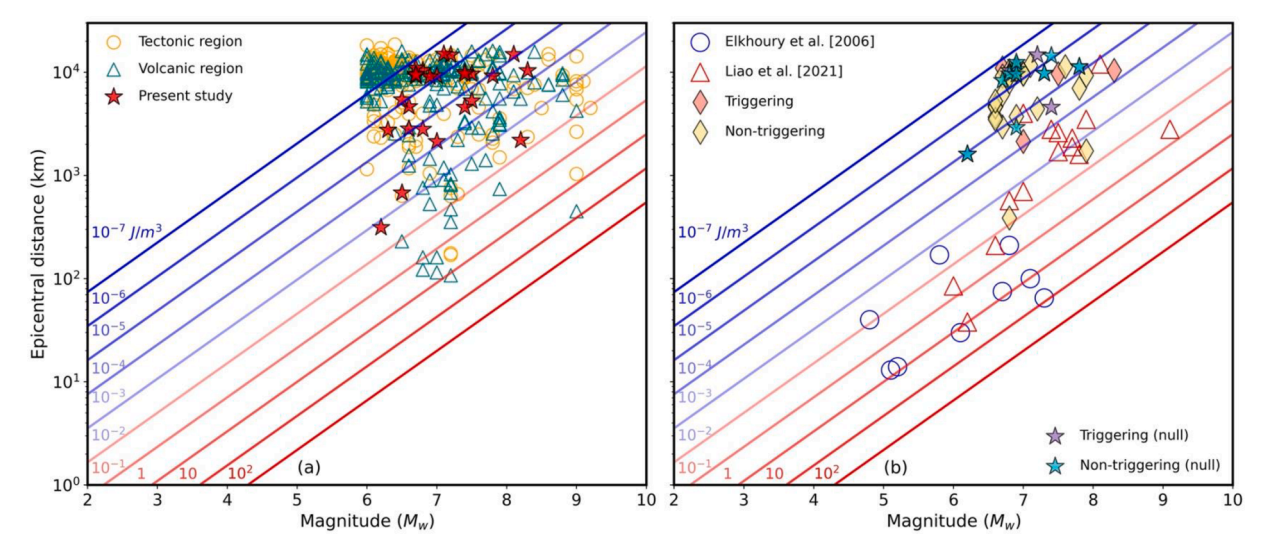


Fig. 5. Theoretical earthquake energy density (E) as a function of magnitude (M) and distance (r) for dynamic triggering and inferred permeability observations, computed via the empirical scaling relationship (log(r) = 0.48 M - 0.33 log(E) - 1.4) proposed by Wang (2007). (a) Comparison between our observations and previous findings of dynamic earthquake triggering in volcanic and tectonic regions (Moran et al., 2004; Miyazawa et al., 2005; Cannata et al., 2010; Yukutake et al., 2013; Wu et al., 2013; Chao et al., 2013; Aiken et al., 2014; Kundu et al., 2016; Mendoza et al., 2016; Cattania et al., 2017; Neves et al., 2018; Fan et al., 2021; Alfaro-Diaz et al., 2020; Pankow et al., 2020). (b) Comparison of changed (diamond) and null (star) inferred permeability observations (triggering and non-triggering cases) with previous observations (Elkhoury et al., 2006; Liao et al., 2021).

respectively during the 2015-2019 period. Whereas after 2019, the proportion of instant/extended and delayed triggering were ~66 % (8/12) and  $\sim 25\%$  (3/12), respectively. To test whether the difference in the proportion of triggering types is statistically significant, we performed a binomial test based on the null hypothesis that the proportion of triggering type is constant and obtained a p-value < 0.05. With this, we reject the null hypothesis and suggest that the rate of instant and delayed triggering significantly differed between the two periods. However, due to unstable hydrothermal vent-fluid temperature data after 2019, we cannot obtain reliable phase lag estimates to constrain the relation of permeability changes with this trend. Nevertheless, the increase in proportion of instant triggering cases after 2019 is consistent with Axial Seamount being critically stressed and hence being more sensitive to temporary increase in Coulomb stress due to passing seismic waves. Our observations are consistent with Bell et al. (2021) who reported an increase in dynamic earthquake triggering intensity during the inflation of the magma reservoir at Sierra Negra volcano due to elevated background stress levels, which is absent during the immediate post-eruption period despite comparable dynamic strain. They conclude that the absence of dynamic earthquake triggering after the eruption is mainly due to a decrease in the background stress state. The strong tidal triggering signal 3-months prior to the 2015 Axial eruption compared to 7 months after also suggests that Axial Seamount becomes more sensitive to earthquake triggering by small stress perturbations when it is critically stressed (Wilcock et al., 2016). Therefore, we suggest that our observations might reflect Axial Seamount becoming more responsive to transient stresses as it inflates and builds up to the next eruption.

Signatures of permeability change following major earthquakes are often used to comprehend the complex interaction of seismic waves and crustal permeability (Johnson et al., 2001; Brodsky et al., 2003; Dziak et al., 2003; Elkhoury et al., 2006; Crone et al., 2011; Wang et al., 2016; Shi et al., 2019; Liao et al., 2021). For instance, Elkhoury et al. (2006) reported that the permeability generally increased with the PGV amplitude, while Shi et al. (2019) observed both increase and decrease in permeability following the passage of seismic waves. Our results show that permeability may either increase, decrease, or remain unchanged following the passage of seismic waves, and it does not appear to correlate with PGV amplitude (Fig. S7). Notably, the proportion of CE accompanied by changed permeability (~70 %) is significantly higher than the null cases (~30 %), in comparison with our randomized test (changed observations ~24 %; null observations ~76 %). This suggests that Axial Seamount's crustal permeability is sensitive to passing seismic waves.

The observation of permeability increase is more pronounced at Axial Seamount in comparison to permeability decrease (Fig. S6). This might be explained by the clogging and unclogging of fractures depending on the azimuthal distribution of the CE, which controls the permeability changes, as discussed by Shi et al. (2019). Following the Shi et al. (2019) interpretation, we also quantify the permeability dependence on the azimuthal distribution of the CE (Fig. S9b; Table S3). We find that the proportion of changed permeability observations is relatively higher for the azimuthal bands which are nearly anti-parallel (~135°  $\pm$  20°; 73.3 %: Table S3) and perpendicular (~240°  $\pm$  20°; 69.2 %: Table S3) to local fault orientation (strike  $\sim$ 330°) (Levy et al., 2018). One possible explanation for the inferred permeability change in fault anti-parallel direction is presumably the unclogging of a favourably oriented fracture network at Axial Seamount (Fig. S8). This would be consistent with Shi et al. (2019) who observed permeability changes in response to seismic waves from earthquakes that are distributed in distinct azimuthal zones and inferred to reflect the clogging and unclogging of fractures (Shi et al., 2018, 2019). Because of the limited number of permeability observations within different azimuthal bands, we can only speculate about the dependence of permeability change on the orientation of incoming seismic waves.

Liao et al. (2021) previously suggested that the difference in the frequency content of seismic waves (e.g., permeability changes being

more sensitive to long-period seismic waves) could explain null permeability observations despite comparable E. We did not observe any apparent dependence of permeability change on the frequency content of the incoming seismic waves at Axial Seamount which is also consistent with the triggering and non-triggering observations (Figs. S6, S8). Based on the empirical relationship between earthquake magnitude, epicentral distance, and energy density E, we further find that our observed permeability changes occur at relatively lower E (down to  $10^{-7}$  J/m³; Fig. 5b) in comparison to previous studies ( $E{\sim}10^{-5}$  J/m³) (Elkhoury et al., 2006; Liao et al., 2021). The lower E threshold is consistent with the E threshold for dynamic earthquake triggering, which suggests that the stress change necessary for dynamic earthquake triggering and permeability changes is comparable. This would be expected if dynamic earthquake triggering and permeability changes are related.

Lastly, we analyze our inferred permeability observations to evaluate the hypothesis that changes in permeability can serve as a mechanism for dynamic earthquake triggering. We report comparable permeability responses for both triggering and non-triggering observations which include increased, decreased, and unchanged permeability records (Fig. 4). This suggests that permeability change might not be a necessary or primary mechanism that controls dynamic earthquake triggering at Axial Seamount. However, there are a few caveats to consider. Firstly, the total number of our inferred permeability observations and dynamic earthquake triggering cases are still relatively limited. Secondly, the non-triggering CE with permeability change may have triggered seismicity at a level that is not resolvable with our earthquake catalog. The permeability of oceanic crust has been shown to vary by several orders of magnitude over a horizontal scale of a few hundred meters (Crone et al., 2011), substantial apparent changes in permeability might result from a slight change in flow path instead of an actual change in permeability structure in the subsurface. Since we only have hydrothermal venting data from a single vent site, the inferred permeability change might also be quite localized, while the spatial variation in permeability over the entire Axial Seamount caldera in response to passing seismic waves might be quite heterogeneous. Finally, the reverse effect of local seismicity causing permeability change cannot be ruled out (Fig. S10). Therefore, an increase in number of observational sites would help better elucidate the complex relationship between permeability change and dynamic earthquake triggering. Nevertheless, our results provide the first observations of permeability changes and increase in seismicity rate in response to transient stresses at a single site which suggest that permeability change can but does not have to be a necessary and/or primary mechanism controlling dynamic earthquake triggering.

#### 5. Conclusions

We provide the first documentation of dynamic earthquake triggering at a submarine volcano during its inflation timeframe. We observe that the triggering susceptibility of Axial Seamount is comparable with other subaerial tectonic and volcanic regions. We did not find any obvious dependence of the triggering rate on the dynamic stress amplitude. Instead, the triggering sensitivity might increase as the volcano builds up towards the next eruption and becomes critically stressed. We find that crustal permeability change can occur in response to passing seismic waves at comparable energy density threshold as that which causes dynamic earthquake triggering. However, we do not find conclusive evidence that measurable permeability change is a primary driver of dynamic earthquake triggering at Axial Seamount. Therefore, we conclude that in addition to Coulomb stress and permeability change, other mechanisms including cascade stress triggering, rate-andstate friction, subcritical crack growth, and triggered creep may also control dynamic earthquake triggering at Axial Seamount.

#### CRediT authorship contribution statement

Adnan Barkat: Writing – original draft, Visualization, Methodology, Investigation, Formal analysis. Yen Joe Tan: Writing – review & editing, Supervision, Project administration, Methodology, Funding acquisition, Conceptualization. Guangyu Xu: Writing – review & editing. Felix Waldhauser: Writing – review & editing. Maya Tolstoy: Writing – review & editing. William S.D. Wilcock: Writing – review & editing.

#### Declaration of competing interest

The authors declare that they have no known competing financial interests or personal relationships that could have appeared to influence the work reported in this paper.

#### Data availability

Data will be made available on request.

#### Data and Resources

The Axial Seamount earthquake catalog was downloaded from database of Lamont-Doherty Earth Observatory, Columbia University (https://www.ldeo.columbia.edu/~felixw/Axial.RTDD/).

The triggering sources catalog was obtained from U.S. Geological Survey (USGS; https://earthquake.usgs.gov/earthquakes/search/). Hydrothermal vent-fluid temperature and tidal loading data were retrieved from Ocean Observatories Initiative (OOI) explorer database (https://dataexplorer.oceanobservatories.org/). All the figures and maps were generated using python and PYGMT. All websites were last accessed in September 2021.

#### Acknowledgements

A. Barkat and Y.J. Tan are supported by National Natural Science Foundation of China Grant Number 42122060 and the Croucher Tak Wah Mak Innovation Award. F. Waldhauser, M. Tolstoy, and W.S.D. Wilcock are supported by National Science Foundation grants OCE-1536320, OCE-0649538, OCE-1536219, OCE-1951448, and OCE-1950996. The authors thank Editor Rebecca Bendick, Editor Chiara Maria Petrone, Andy Bell and an anonymous reviewer for their constructive comments and suggestions.

#### Supplementary materials

Supplementary material associated with this article can be found, in the online version, at doi:10.1016/j.epsl.2024.118625.

#### References

- Aiken, C., Meng, X., Hardebeck, J., 2018. Testing for the predictability of dynamically triggered earthquakes in The Geysers geothermal field. Earth Planet. Sci. Lett. 486 (129), 140. https://doi.org/10.1016/j.epsl.2018.01.015.
- Aiken, C., Peng, Z., 2014. Dynamic triggering of microearthquakes in three geothermal/volcanic regions of California. J. Geophys. Res. 119 (9), 6992–7009. https://doi.org/10.1002/2014JB011218.
- Alfaro-Diaz, R., Velasco, A.A., Pankow, K.L., Kilb, D., 2020. Optimally oriented remote triggering in the Coso geothermal region. J. Geophys. Res. 125 (8) https://doi.org/ 10.1029/2019JB019131 e2019JB019131.
- $Allen, R.V., 1978. \ Automatic earthquake recognition and timing from single traces. Bull. Seismol. Soc. Am. 68 (5), 1521–1532. \ https://doi.org/10.1785/BSSA0680051521.$
- Azaria, M., Hertz, D., 1984. Time delay estimation by generalized cross correlation methods. IEEE Trans. Acoust. Speech Signal Process 32 (2), 280–285. https://doi. org/10.1109/TASSP.1984.1164314.
- Baillard, C., Crawford, W.C., Ballu, V., Hibert, C., Mangeney, A., 2014. An automatic kurtosis-based P-and S-phase picker designed for local seismic networks. Bull. Seismol. Soc. Am. 104 (1), 394–409. https://doi.org/10.1785/0120120347.
- Barreyre, T., Escartin, J., Sohn, R., Cannat, M., 2014. Permeability of the Lucky Strike deep-sea hydrothermal system: constraints from the poroelastic response to ocean

- tidal loading. Earth Planet. Sci. Lett. 408, 146–154. https://doi.org/10.1016/j.epsl.2014.09.049.
- Barreyre, T., Parnell-Turner, R., Wu, J.N., Fornari, D.J., 2022. Tracking crustal permeability and hydrothermal response during seafloor eruptions at the East Pacific Rise, 9 50'N. Geophys. Res. Lett. 49 (3) https://doi.org/10.1029/2021GL095459 e2021GL095459.
- Barreyre, T., Sohn, R.A., 2016. Poroelastic response of mid-ocean ridge hydrothermal systems to ocean tidal loading: implications for shallow permeability structure. Geophys. Res. Lett. 43 (4), 1660–1668. https://doi.org/10.1002/2015GL066479.
- Bell, A.F., Hernandez, S., McCloskey, J., Ruiz, M., LaFemina, P.C., Bean, C.J., Möllhoff, M., 2021. Dynamic earthquake triggering response tracks evolving unrest at Sierra Negra volcano, Galápagos Islands. Sci. Adv. 7 (39) https://doi.org/ 10.1126/sciadv.abh0894 eabh0894.
- Brodsky, E.E., Karakostas, V., Kanamori, H., 2000. A new observation of dynamically triggered regional seismicity: earthquakes in Greece following the August 1999 Lzmit, Turkey earthquake. Geophys. Res. Lett. 27 (17), 2741–2744. https://doi.org/ 10.1029/2000GL011534.
- Brodsky, E.E., Prejean, S.G., 2005. New constraints on mechanisms of remotely triggered seismicity at Long Valley Caldera. J. Geophys. Res. 110 (B4) https://doi.org/
- Brodsky, E.E., Roeloffs, E., Woodcock, D., Gall, I., Manga, M., 2003. A mechanism for sustained groundwater pressure changes induced by distant earthquakes. J. Geophys. Res. 108 (B8) https://doi.org/10.1029/2002JB002321.
- Cannata, A., Di Grazia, G., Montalto, P., Aliotta, M., Patanè, D., Boschi, E., 2010. Response of Mount Etna to dynamic stresses from distant earthquakes. J. Geophys. Res. (B12), 115. https://doi.org/10.1029/2010JB007487.
- Cattania, C., McGuire, J.J., Collins, J.A., 2017. Dynamic triggering and earthquake swarms on East Pacific Rise transform faults. Geophys. Res. Lett. 44 (2), 702–710. https://doi.org/10.1002/2016GL070857.
- Chadwick Jr, W.W., Wilcock, W.S., Nooner, S.L., Beeson, J.W., Sawyer, A.M., Lau, T.K., 2022. Geodetic monitoring at Axial Seamount since its 2015 eruption reveals a waning magma supply and tightly linked rates of deformation and seismicity. Geochem. Geophys. Geosyst. 23 (1) https://doi.org/10.1029/2021GC010153 e2021GC010153.
- Chao, K., Peng, Z., Gonzalez-Huizar, H., Aiken, C., Enescu, B., Kao, H., Matsuzawa, T., 2013. A global search for triggered tremor following the 2011M w 9.0 Tohoku earthquake. Bull. Seismol. Soc. Am. 103 (2B), 1551–1571. https://doi.org/10.1785/ 0120120171.
- Crone, T.J., Wilcock, W.S., 2005. Modeling the effects of tidal loading on mid-ocean ridge hydrothermal systems. Geochem. Geophys. Geosyst. 6 (7) https://doi.org/ 10.1029/2004GC000905.
- Crone, T.J., Tolstoy, M., Stroup, D.F., 2011. Permeability structure of young ocean crust from poro-elastically triggered earthquakes. Geophys. Res. Lett. 38 (5) https://doi. org/10.1029/2011GL046820.
- Dziak, R.P., Chadwick Jr, W.W., Fox, C.G., Embley, R.W., 2003. Hydrothermal temperature changes at the southern Juan de Fuca Ridge associated with MW 6.2 Blanco Transform earthquake. Geology 31 (2), 119–122. https://doi.org/10.1130/ 0091-7613
- Elkhoury, J.E., Brodsky, E.E., Agnew, D.C., 2006. Seismic waves increase permeability. Nature 441 (7097), 1135–1138. https://doi.org/10.1038/nature04798.
- Fan, W., Barbour, A.J., Cochran, E.S., Lin, G., 2021. Characteristics of frequent dynamic triggering of microearthquakes in Southern California. J. Geophys. Res. 126 (1) https://doi.org/10.1029/2020JB020820 e2020JB020820.
- Freed, A.M., 2005. Earthquake triggering by static, dynamic, and postseismic stress transfer. Annu. Rev. Earth Planet. Sci. 33, 335–367. https://doi.org/10.1146/ annurey.earth.33.092203.122505.
- Gonzalez-Huizar, H., Velasco, A.A., 2011. Dynamic triggering: stress modeling and a case study. J. Geophys. Res. 116 (B2) https://doi.org/10.1029/2009JB007000.
- Gomberg, J., 2001. The failure of earthquake failure models. J. Geophys. Res. 106 (B8), 16253–16263. https://doi.org/10.1029/2000JB000003.
- Harrington, R.M., Brodsky, E.E., 2006. The absence of remotely triggered seismicity in Japan. Bull. Seismol. Soc. Am. 96 (3), 871–878. https://doi.org/10.1785/ 0120050076
- Hill, D.P., Reasenberg, P.A., Michael, A., Arabaz, W.J., Beroza, G., Brumbaugh, D., Zollweg, J., 1993. Seismicity remotely triggered by the magnitude 7.3 Landers, California, earthquake. Science 260 (5114), 1617–1623. https://doi.org/10.1126/ science.260.5114.1617.
- Hill, D.P., 2008. Dynamic stresses, Coulomb failure, and remote triggering. Bull. Seismol. Soc. Am. 98 (1), 66–92. https://doi.org/10.1785/0120070049.
- Ide, S., Yabe, S., Tanaka, Y., 2016. Earthquake potential revealed by tidal influence on earthquake size–frequency statistics. Nat. Geosci 9 (11), 834–837. https://doi.org/ 10.1038/ngeo2796.
- Johnson, H.P., Dziak, R.P., Fisher, C.R., Fox, C.G., Pruis, M.J., 2001. Earthquakes' impact on hydrothermal systems may be far-reaching. Eos Trans. Am. Geophys. Union 82 (21), 233–236. https://doi.org/10.1029/01EO00127.
- Johnson, P.A., Jia, X., 2005. Nonlinear dynamics, granular media and dynamic earthquake triggering. Nature 437 (7060), 871–874. https://doi.org/10.1038/ nature04015.
- Kelley, D.S., Delaney, J.R., Juniper, S.K., 2014. Establishing a new era of submarine volcanic observatories: cabling axial seamount and the endeavour segment of the Juan de Fuca Ridge. Mar. Geol. 352, 426–450. https://doi.org/10.1016/j. margeo.2014.03.010.
- Kinoshita, C., Kano, Y., Ito, H., 2015. Shallow crustal permeability enhancement in central Japan due to the 2011 Tohoku earthquake. Geophys. Res. Lett 42 (3), 773–780. https://doi.org/10.1002/2014GL062792.

- Kinoshita, M., Kitada, K., Nozaki, T., 2022. Tidally modulated temperature observed atop a drillsite at the Noho hydrothermal site, mid-Okinawa Trough. J. Geophys. Res. 127 (7) https://doi.org/10.1029/2021JB023923 e2021JB023923.
- Klein, F.W., 2002. User's guide to HYPOINVERSE-2000, a Fortran program to solve for earthquake locations and magnitudes (No. 2002–171). U.S. Geological Survey. https://doi.org/10.3133/ofr02171.
- Kundu, B., Ghosh, A., Mendoza, M., Bürgmann, R., Gahalaut, V.K., Saikia, D., 2016. Tectonic tremor on Vancouver Island, Cascadia, modulated by the body and surface waves of the Mw 8.6 and 8.2, 2012 East Indian Ocean earthquakes. Geophys. Res. Lett. 43 (17), 9009–9017. https://doi.org/10.1002/2016GL069755.
- Levy, S., Bohnenstiehl, D.R., Sprinkle, P., Boettcher, M.S., Wilcock, W.S.D., Tolstoy, M., Waldhauser, F., 2018. Mechanics of fault reactivation before, during, and after the 2015 eruption of Axial Seamount. Geology 46 (5), 447–450. https://doi.org/ 10.1130/G39978.1.
- Liao, X., Shi, Y., Liu, C.P., Wang, G., 2021. Sensitivity of permeability changes to different earthquakes in a fault zone: possible evidence of dependence on the frequency of seismic waves. Geophys. Res. Lett. 48 (9) https://doi.org/10.1029/ 2021GL092553 e2021GL092553.
- Moran, S.C., Power, J.A., Stihler, S.D., Sánchez, J.J., Caplan-Auerbach, J., 2004. Earthquake triggering at Alaskan volcanoes following the 3 November 2002 Denali fault earthquake. Bull. Seismol. Soc. Am. 94 (6B), S300–S309. https://doi.org/ 10.1285/0120040608
- Matthews, M.V., Reasenberg, P.A., 1988. Statistical methods for investigating quiescence and other temporal seismicity patterns. Pure Appl. Geophys. 126, 357–372. https://doi.org/10.1007/BF00879003.
- Marsan, D., Wyss, M., 2011. Seismicity rate changes, Community Online Resource for Statistical Seismicity Analysis. https://doi.org/10.5078/corssa-25837590.
- Marsan, D., Lengline, O., 2008. Extending earthquakes' reach through cascading. Science 319 (5866), 1076–1079. https://doi.org/10.1126/science.1148783.
- Manga, M., Beresnev, I., Brodsky, E.E., Elkhoury, J.L., Elsworth, D., Ingebritsen, S.E., Wang, C.Y., 2012. Changes in permeability caused by transient stresses: field observations, experiments, and mechanisms. Rev. Geophys. 50 (2) https://doi.org/ 10.1029/2011RG000382.
- Mendoza, M.M., Ghosh, A., Rai, S.S., 2016. Dynamic triggering of small local earthquakes in the central Himalaya. Geophys. Res. Lett. 43 (18), 9581–9587. https://doi.org/10.1002/2016GL069969.
- Miyazawa, M., Nakanishi, I., Sudo, Y., Ohkura, T., 2005. Dynamic response of frequent tremors at Aso volcano to teleseismic waves from the 1999 Chi-Chi, Taiwan earthquake. J. Volcanol. Geotherm. Res. 147 (1–2), 173–186. https://doi.org/ 10.1016/j.jvolgeores.2005.03.012.
- Neves, M., Custódio, S., Peng, Z., Ayorinde, A., 2018. Earthquake triggering in southeast Africa following the 2012 Indian Ocean earthquake. Geophys. J. Int. 212 (2), 1331–1343. https://doi.org/10.1093/gji/ggx462.
- Pankow, K.L., Kilb, D., 2020. Going beyond rate changes as the sole indicator for dynamic triggering of earthquakes. Sci. Rep. 10 (1), 4120. https://doi.org/10.1038/ s41598-020-60988-2.
- Parsons, T., 2005. A hypothesis for delayed dynamic earthquake triggering. Geophys. Res. Lett. 32 (4) https://doi.org/10.1029/2004GL021811.
- Parsons, T., Velasco, A.A., 2011. Absence of remotely triggered large earthquakes beyond the mainshock region. Nat. Geosci. 4 (5), 312–316. https://doi.org/10.1038/
- Peng, Z., Hill, D.P., Shelly, D.R., Aiken, C., 2010. Remotely triggered microearthquakes and tremor in central California following the 2010 Mw 8.8 Chile earthquake. Geophys. Res. Lett. (24), 37. https://doi.org/10.1029/2010GL045462.
- Prejean, S.G., Hill, D.P., 2018. The influence of tectonic environment on dynamic earthquake triggering: a review and case study on Alaskan volcanoes.

  Tectonophysics 745, 293–304. https://doi.org/10.1016/j.tecto.2018.08.007.
- Savage, H.M., Marone, C., 2008. Potential for earthquake triggering from transient deformations. J. Geophys. Res. 113 (B5) https://doi.org/10.1029/2007JB005277.
- Scholz, C.H., Tan, Y.J., Albino, F., 2019. The mechanism of tidal triggering of earthquakes at mid-ocean ridges. Nat Commun 10 (1), 2526. https://doi.org/ 10.1038/s41467-019-10605-2.
- Seropian, G., Kennedy, B.M., Walter, T.R., Ichihara, M., Jolly, A.D., 2021. A review framework of how earthquakes trigger volcanic eruptions. Nat. Commun. 12 (1), 1004. https://doi.org/10.1038/s41467-021-21166-8.
- Shelly, D.R., Peng, Z., Hill, D.P., Aiken, C., 2011. Triggered creep as a possible mechanism for delayed dynamic triggering of tremor and earthquakes. Nat. Geosci 4 (6), 384–388. https://doi.org/10.1038/ngeo1141.

- Shi, Z., Zhang, S., Yan, R., Wang, G., 2018. Fault zone permeability decrease following large earthquakes in a hydrothermal system. Geophys. Res. Lett. 45 (3), 1387–1394. https://doi.org/10.1002/2017GL075821.
- Shi, Y., Liao, X., Zhang, D., Liu, C.P., 2019. Seismic waves could decrease the permeability of the shallow crust. Geophys. Res. Lett. 46 (12), 6371–6377. https:// doi.org/10.1029/2019GL081974.
- Stark, M.A., Davis, S.D., 1996. Remotely triggered microearthquakes at The Geysers geothermal field, California. Geophys. Res. Lett. 23 (9), 945–948. https://doi.org/ 10.1029/96GL00011.
- Tan, Y.J., Waldhauser, F., Tolstoy, M., Wilcock, W.S., 2019. Axial Seamount: periodic tidal loading reveals stress dependence of the earthquake size distribution (b value). Earth Planet. Sci. Lett. 512, 39–45. https://doi.org/10.1016/j.epsl.2019.01.047.
- Tan, Y.J., Tolstoy, M., Waldhauser, F., Bohnenstiehl, D.R., 2018. Tidal triggering of microearthquakes over an eruption cycle at 9 50'N East Pacific Rise. Geophys. Res. Lett. 45 (4), 1825–1831. https://doi.org/10.1002/2017GL076497.
- Tanaka, S., 2010. Tidal triggering of earthquakes precursory to the recent Sumatra megathrust earthquakes of 26 December 2004 (Mw 9.0), 28 March 2005 (Mw 8.6), and 12 September 2007 (Mw 8.5). Geophys. Res. Lett. 37 (2) https://doi.org/ 10.1029/2009G1041581
- Tolstoy, M., Vernon, F.L., Orcutt, J.A., Wyatt, F.K., 2002. Breathing of the seafloor: tidal correlations of seismicity at Axial volcano. Geology 30 (6), 503–506. https://doi. org/10.1130/0091-7613.
- van der Elst, N.J., Brodsky, E.E., 2010. Connecting near-field and far-field earthquake triggering to dynamic strain. J. Geophys. Res. 115 (B7) https://doi.org/10.1029/
- van der Elst, N.J., Savage, H.M., Keranen, K.M., Abers, G.A., 2013a. Enhanced remote earthquake triggering at fluid-injection sites in the midwestern United States. Science 341 (6142), 164–167. https://doi.org/10.1126/science.1238948.
- van der Elst, N.J., Brodsky, E.E., Lay, T., 2013b. Remote triggering not evident near epicentres of impending great earthquakes. Bull. Seismol. Soc. Am. 103 (2B), 1522–1540. https://doi.org/10.1785/0120120126.
- Velasco, A.A., Hernandez, S., Parsons, T., Pankow, K., 2008. Global ubiquity of dynamic earthquake triggering. Nat. Geosci. (1), 375–379. https://doi.org/10.1038/ngeo204.
- Waldhauser, F., Wilcock, W.S.D., Tolstoy, M., Baillard, C., Tan, Y.J., Schaff, D.P., 2020. Precision seismic monitoring and analysis at Axial Seamount using a real-time double-difference system. J. Geophys. Res. 125 (5) https://doi.org/10.1029/ 2019JB018796 e2019JB018796.
- Waldhauser, F., 2009. Near-real-time double-difference event location using long-term seismic archives, with application to Northern California. Bull. Seismol. Soc. Am. 99 (5), 2736–2748. https://doi.org/10.1785/0120080294.
- Wang, C.Y., Liao, X., Wang, L.P., Wang, C.H., Manga, M., 2016. Large earthquakes create vertical permeability by breaching aquitards. Water Resour. Res. 52 (8), 5923–5937. https://doi.org/10.1002/2016WR018893.
- Wang, K., Davis, E.E., 1996. Theory for the propagation of tidally induced pore pressure variations in layered subseafloor formations. J. Geophys. Res.: Solid Earth 101 (B5), 11483–11495. https://doi.org/10.1029/96JB00641.
- Wilcock, W.S., Tolstoy, M., Waldhauser, F., Garcia, C., Tan, Y.J., Bohnenstiehl, D.R., Mann, M.E., 2016. Seismic constraints on caldera dynamics from the 2015 Axial Seamount eruption. Science 354 (6318), 1395–1399. https://doi.org/10.1126/ science.aah5563.
- Wilcock, W.S., Dziak, R.P., Tolstoy, M., Chadwick Jr, W.W., Nooner, S.L., Bohnenstiehl, D.R., Mann, M.E., 2018. The recent volcanic history of Axial Seamount: geophysical insights into past eruption dynamics with an eye toward enhanced observations of future eruptions. Oceanography 31 (1), 114–123. https:// doi.org/10.5670/oceanog.2018.117.
- Wu, C., Peng, Z., Wang, W., Chen, Q.F., 2011. Dynamic triggering of shallow earthquakes near Beijing, China. Geophys. J. Int. 185 (3), 1321–1334. https://doi.org/10.1111/ i 1365-246X 2011.05002 x
- Xu, G., Larson, B.I., Bemis, K.G., Lilley, M.D., 2017. A preliminary 1-D model investigation of tidal variations of temperature and chlorinity at the Grotto mound, Endeavour Segment, Juan de Fuca Ridge. Geochem. Geophys. Geosyst. 18 (1), 75–92. https://doi.org/10.1002/2016GC006537.
- Yun, N., Zhou, S., Yang, H., Yue, H., Zhao, L., 2019. Automated detection of dynamic earthquake triggering by the high-frequency power integral ratio. Geophys. Res. Lett. 46 (22), 12977–12985. https://doi.org/10.1029/2019GL083913.
- Yukutake, Y., Miyazawa, M., Honda, R., Harada, M., Ito, H., Sakaue, M., Yoshida, A., 2013. Remotely triggered seismic activity in Hakone volcano during and after the passage of surface waves from the 2011 M9. 0 Tohoku-Oki earthquake. Earth Planet. Sci. Lett. 373, 205–216. https://doi.org/10.1016/j.epsl.2013.05.004.